



Particulate patterns generated by liquid templates

Diego Barba Maggi^{a,b,1}, Román Martino^{a,1}, Marta Rosen^{a,1}, Marcelo Piva^{a,1}, Alejandro Boschan^{a,*,1}

^a Facultad de Ingeniería, Grupo de Medios Porosos, Universidad de Buenos Aires, Paseo Colón 850, (C1063ACV), Buenos Aires, Argentina

^b Escuela Superior Politécnica de Chimborazo, ESPOCH, Panamericana Sur Km 1 1/2, Riobamba, Ecuador

ARTICLE INFO

Article history:

Received 27 September 2019

Received in revised form 26 February 2020

Accepted 1 March 2020

Available online 03 March 2020

Keywords:

Templates

Particles

Tissue

Pattern

Bed

Liquid

ABSTRACT

We characterize the assembly of microscopic particles in patterned beds. The particles are immersed in a liquid template generated by vibration. We study, at the same time, the waves in the liquid surface, and the topography of the bed. Results show that the surface waves are travelling, harmonic and capillary waves, in contrast with previous studies that examined Faraday subharmonic waves. The patterned bed presents an alternation of annular ridges and troughs, with a characteristic lengthscale similar to the surface wavelength. The amplitude of the variation of the bed thickness increases as the mean bed thickness increases, and as the vibration frequency decreases; this is explained in terms of a Shields number that depends on both variables. In turn, the localization efficiency of the particles decreases with the bed thickness but increases with the pattern characteristic lengthscale. We discuss assembly design and compare with dry granular systems.

© 2020 Elsevier B.V. All rights reserved.

1. Introduction

The appearance of patterns in particulate systems has been studied since many years [1,2]. Generated by vibrations, shear, buoyancy and other perturbations, they were observed both when particles are dry or immersed in a liquid. From the technological point of view, the ability to assemble nano- and microscopic particles by localizing them into arrays or patterned films over a substrate is of interest in the development of new materials, such as colloidal crystals, and in several biological and medical applications [3,4] like tissue engineering [5].

Different methods based on electric [6], magnetic [7], and acoustic [8,9] fields have been used to control particle position and orientation. For example, convective self-assembly [10] uses capillary forces and evaporation to produce patterned particulate films.

Moreover, the use of liquid templates makes it possible to rapidly reconfigure the structure once a first assembly is achieved, an advantageous feature for technological applications. This technique consists in creating flow structures in a liquid so they interact with the particles, mobilizing them to specific positions in a substrate. One way of generating liquid templates, is to apply a controlled vibration to a liquid layer, either by using acoustic waves or by direct mechanical stimulus.

Takagi et al. [11] used this technique to produce cylindrical patterns of endothelial cells in very short times. The localization of deposited talc particles by standing waves generated by vibration was studied by Wright and Saylor [12], who found that the lengthscale imposed by

the vibration frequency strongly influenced that of the patterns despite some discrepancies. Saylor and Kinard [13] studied numerically how the particle diameter and liquid layer thickness modified the localization efficiency. Chen et al. [14] studied a variety of reconfigurable patterns in which spheroids assembled in arrays of lines, demonstrating the versatility of the technique. They observed that, as the number of loaded spheroids increased, the width of these lines increased linearly, then implying a decrease of the localization efficiency. Later [15], the authors created stem cell-derived cardiac tissue using liquid templates. All these works assumed that the mechanism driving the pattern formation was the drift of the particles to the nodes of Faraday waves, focusing mainly on the particle patterns. From a basic research perspective, it has been shown that the coupling of the particles with a fluid is intimately related with the appearance of structures [16,17]. Actually, this type of coupling was intensively studied in the framework of coastal sciences and hydrology [18], in natural landscapes and lab experiments [19,20]. The oscillatory shear stress generated by the surface waves propagates downwards, and, as the shear force exerted on the bed particles exceeds a certain critical value, the motion of the particles gives rise to the formation of patterns in the form of ripples and dunes [21].

Finally, considering the liquid template configuration employed by the above mentioned investigations, we recall that harmonic capillary waves may coexist with subharmonic Faraday waves [22] in the flow field driven by the vertical oscillation of a thin layer of a pure viscous liquid. Taking also into account the interaction among the particles, the liquid and a vibrating container, that involves at least three phases, many types of interactions, and several degrees of freedom [23,24], achieving a comprehensive description of the assembly process using liquid templates is difficult. It should be also mentioned that vibration does not

* Corresponding author.

E-mail address: abosch@fi.uba.ar (A. Boschan).

¹All authors contributed equally.

only generate the flow structure in the liquid that interacts with the particles, but it is also expected to directly influence the bulk structure of the bed [25–27] by mechanical contact with the container.

Indeed, for dry granular systems, it has been shown that vibration affects the structure of packings: 1D vibration causes compaction of the random bed structure, but, under certain conditions, 2D and 3D vibrations can force the particles to assemble into compact crystalline structures, such as hexagonal close-packed or face-centered cubic [28–30]. Although this phenomenon has not been observed for particulate beds immersed in a liquid, that always maintain a random disordered structure [26,31,32], vibration can still generate a considerable degree of compaction, which affects the stability of the bed.

These issues motivate the present work, whose objective is twofold: First, to study, at the same time, the waves in the liquid (that conform the template), and the patterns that develop in the particulate bed, in order to improve the understanding of the underlying mechanisms. Second, to enhance the existing description of assembly process using by liquid templates, by reproducing topographic maps of the beds, and by assessing the volumetric localization efficiency.

We analyze first the nature of the waves at the free surface, comparing their wavelength to the characteristic length of the patterned bed. The bed topography is then studied by using a photometric technique, varying the two parameters that control the structure of the bed [12,14,15]: the mean bed thickness (the quantity of particles in the bed), and the vibration frequency, that sets the lengthscale. This technique allows us to study aspects of the patterned beds that weren't accessible in the previous studies that used 2D descriptions.

The paper is organized as follows: Section 2 presents the materials and the experimental device, while Section 3 develops the experimental methodology. The results are presented in Section 4, and discussed in Section 5.

On the other hand, Appendix A explains the choice of the vibration parameters, while Appendix B presents the photometric technique used to obtain the bed topography.

2. Experimental setup

The experimental device was designed so that imaging of both the free surface and the patterned bed could be performed. Fig. 1 shows the experimental configuration.

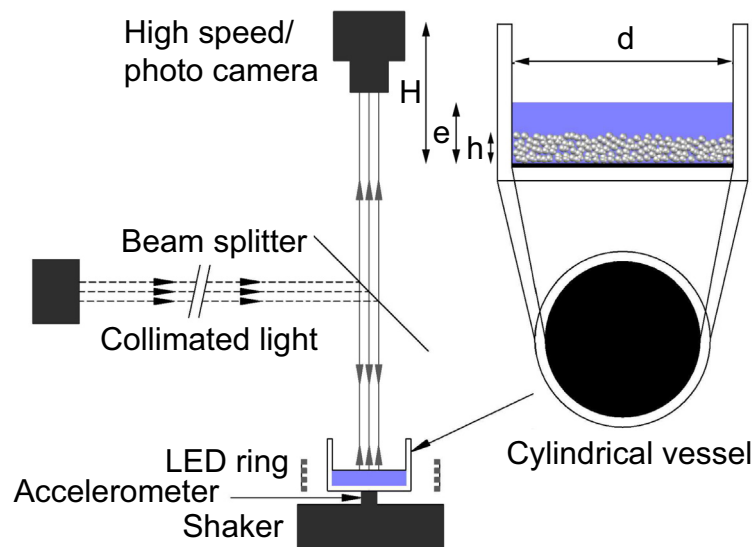


Fig. 1. Scheme of the experimental device. A beam splitter was used to acquire images of the light intensity reflected in the free surface with a fast camera and a collimated light. On the other hand, imaging of the patterned bed at the bottom of the container was performed by using a led ring that surrounded the container illuminating inwards and a photo camera with high spatial resolution.

A Brüel and Kjaer V406 LDS vibrator (5 Hz to 9 KHz, maximum acceleration 50 g) was held by an anti-vibration table, the plexiglass container was attached to the vibrator by using a cylindrical steel piece with screws in both ends. The cylindrical container was attached to the axis of an electromagnetic shaker, which is, in turn, held by an anti-vibration table. The shaker was fed with a sinusoidal signal from a power amplifier (MAXD, Model 4210) driven by a function generator (GW-INSTEK, Model 8219A). An accelerometer (Analog Devices ADXL325, ± 5 g, sensitivity 174 mV/g), attached to the body of the container, makes it possible to monitor the resulting vibration acceleration Γ and frequency f with an oscilloscope.

The container weighted 146 g, its inner diameter $d = 78$ mm, and its inner height $H = 45$ mm. Because pattern visualization close to the center of the container was poor, a circular crown region (ROI) of internal radius 8 mm and external radius 24 mm (extended to 39 mm for the free surface) was used. This also helped avoiding border effects caused by the container inner walls.

Two led circular rings of 140 mm of diameter surrounded the container and illuminated inwards; a plastic diffuser served to homogenize their light. Imaging of the particle patterns was performed with a Nikon D90 (4 MP) photo camera. On the other hand, imaging of the free surface was performed by using the beam splitter of Fig. 1, with a collimated light source, with a Basler A640–750 high-speed camera (500 fps), or, with a Nikon D90 photo camera (4 MP) sincronized with a strobe light.

The liquid template was a solution of glycerol in water (9 % m/m), with a small amount of SDS surfactant was added to avoid particle aggregation. Its interfacial tension was 45 Dyn/cm as measured in a Kruss Tensiometer, Model K8, and its density $\rho_l = 1.03$ g/cm³. The particles were dispersed in this solution to form mixtures with particle volume fractions $\Phi \equiv \frac{V_{part}}{V_{part} + V_{liq}}$ ranging from 2% to 10%.

We employed monodisperse polystyrene spheres (MicroBeads) of radius $a = 20$ μ m and density $\rho_p = 1.05$ g/cm³. A characterization of the radius and sphericity of the particles can be found in Fig. 2. In the Table 1 shows the values of the experimental parameters.

3. Experimental procedure

As explained in Sec. 1, the two main parameters that are known to control the structure of the patterned beds are quantity of particles

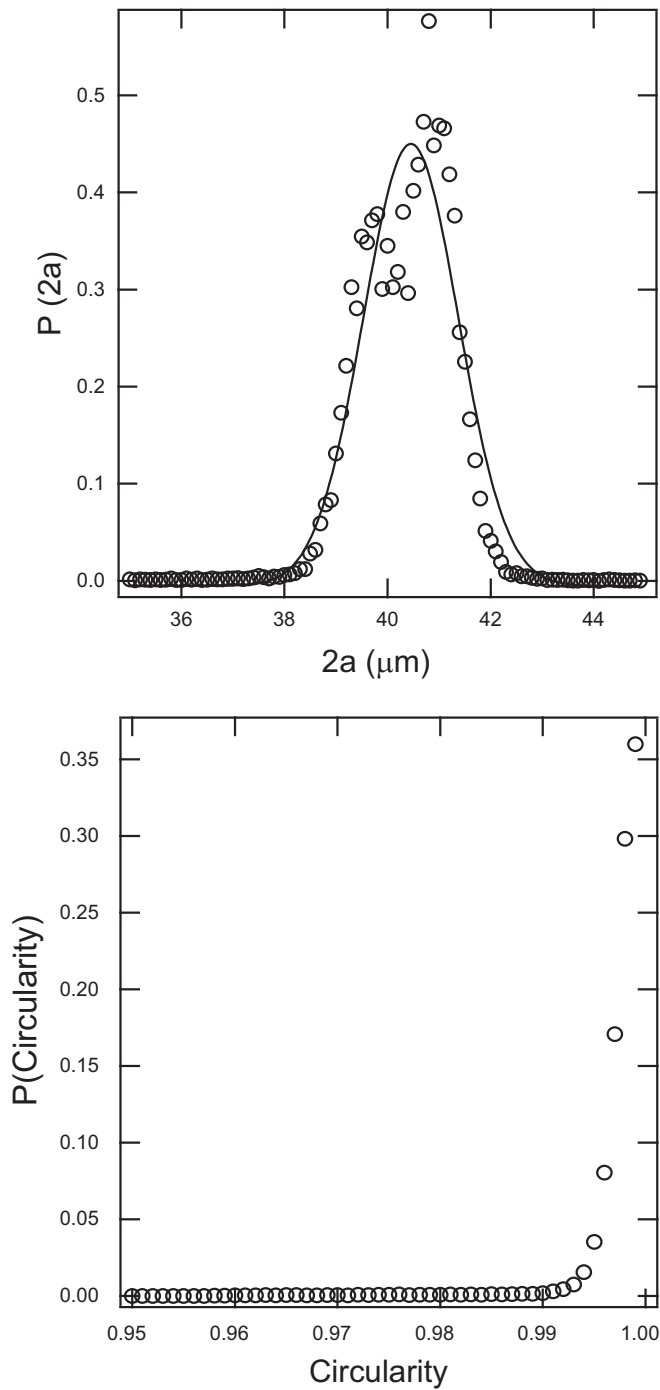


Fig. 2. Characterizations of the polystyrene particles used in the experiments. Top: histogram showing the diameter probability, solid line in top is a gaussian fit. Bottom: histogram showing the circularity probability.

Table 1
Definition of constants of liquid, particles and vessel.

Experimental parameter	Symbol (Unit)	Value
Liquid density	ρ_l (g/cm^3)	1.03
Liquid absolute viscosity	η ($\text{Pa}\cdot\text{s}$)	0.001
Liquid kinematic viscosity	ν (cm^2/s)	0.001
Liquid surface tension	τ (Dyn/cm)	45
Particle density	ρ_p (g/cm^3)	1.05
Particles radius	a (μm)	20
Inner container diameter	d (cm)	7.8
Inner container height	H (cm)	4.5

(defined by the target assembly or structure one wants to create) and the vibration frequency (that imposes a length scale). In experiment A, the patterned beds where studied varying the mean bed thickness (the volume fraction Φ of the mixture samples i.e. the total quantity of particles). Table 2 characterizes the composition of the samples, with the corresponding mean bed thickness, expressed in mm , and in terms of the particle radius a . For this experiment, the vibration frequency was set to 65 Hz and the reduced acceleration Γ (the measured acceleration divided by the gravity acceleration) to 1.03, with a vibration amplitude of 0.061 cm. We recall that the vibration amplitude is related to Γ as $A = \frac{g \Gamma}{(2\pi f)^2}$.

In experiment B, the vibration frequencies and accelerations of Table 3 were imposed to the container, using sample N° 2 of Table 2. The resulting vibration amplitudes of the container is also listed. The choice of the vibration parameters is explained in Appendix A.

In all cases, the samples had a volume of 9 ml, with a mixture layer thickness e of 1.88 mm. This value of the thickness provided the clearest patterns.

The procedure used to obtain patterned beds from the mixture samples for both experiments, depicted in Fig. 3, was the following:

a) The mixtures were prepared in an external reservoir, where they were homogenized by vigorous stirring (the relatively low values of Φ made homogenization by stirring efficient). Then, a 9 ml sample was rapidly transferred to the container. There, the particles settled freely under the action of gravity.

b) Then the container was vibrated during 30 s at $f = 65$ Hz and $\Gamma = 2.3$, attaining a non-stationary chaotic regime, that strongly stirred and agitated the sample, resuspending the particles into a visibly homogeneous mixture. The different regimes are developed in Appendix A.

c) Then vibration was turned off for 240 s to let the particles settle again [15], obtaining a uniform bed of thickness h . To verify the uniformity of the bed thickness, the radial intensity profiles were compared with those of layers of milk, with good agreement. This is the initial state of our experiments.

d) Finally, to generate the bed patterning, vibration was set to $f = 65$ Hz and $\Gamma = 1.03$, for experiment A, and to the values of Table 2, for experiment B.

Under these conditions, after approx. 150–200 s, the uniform beds evolved gradually into a steady-state consisting in an alternation, in the radial direction, of ridges and troughs, concentric with the center of the container. These were visualized by the camera as a concentric succession of lighter (ridges) and darker (troughs) rings, the distance between two consecutive lighter rings defining a pattern wavelength λ_p .

In turn, after a short transient of approx. 5 s, the surface waves, as well concentric, reached a steady-state in which they travelled inwards from the container walls to its center, presenting a well defined wavelength λ_w , that remained unaffected by the presence of particles.

Imaging of both was performed, then, after 400 s (the vibration was stopped to acquire images of the patterned bed).

The upper half of Fig. 4 shows the steady-state of the patterned bed, while the lower half shows the surface waves. The characteristic

Table 2
Characteristics of the mixture samples used in experiment A: the mean bed thickness $\langle h \rangle$ is given in mm, and also in terms of the particle radius a , as $\langle h' \rangle$. Note that the free surface is located at $\langle h \rangle/a \sim 94$. The vibration frequency was set to 65 Hz, the reduced acceleration to 1.03, and amplitude 0.061 cm.

Sample. N°	m_p (g)	m_f (g)	Φ	$\langle h \rangle$ (mm)	$\langle h' \rangle = \langle h \rangle/a$
1	0.189	8.979	2%	0.064	2.14
2	0.378	8.796	4%	0.129	4.96
3	0.567	8.612	6%	0.193	7.65
4	0.756	8.429	8%	0.257	10.02
5	0.945	8.246	10%	0.321	12.76

Table 3

Vibration frequencies, reduced accelerations Γ , and amplitudes A employed in experiment B.

Frequency f (Hz)	Red. Acceleration Γ	Amplitude A (cm)
60	1.00	0.069
65	1.03	0.061
80	1.20	0.047
120	1.90	0.033
140	2.40	0.030
200	3.99	0.024

lengthscale of the patterned bed λ_p is given by the ridge-to-ridge distance, while the wavelength of the surface waves (crest-to-crest) is λ_w .

Alternative tests were performed with the vibration on ($f = 65$ Hz and $\Gamma = 1.03$) during step c). Notably, steady state particle patterns achieved with both methods were impossible to distinguish.

Details of the calibration used for mapping local light intensity onto bed thickness are presented in Appendix B.

As for the structure of the bed, in the absence of vibration a random loose packing (RLP) configuration is expected for spheres settling in a liquid [33], with a particle volume fraction Φ approaching a value of

0.56–0.58 within the bed. Without considering the surface flow structures, vibration typically generates a slight compaction of the bed [26,31].

4. Results

4.1. Nature of the surface waves and relation with the patterned beds

We analyze first the nature of the waves in the liquid free surface. Fig. 5 shows a spatiotemporal diagram of the normalized light intensity reflected by the liquid surface, obtained at approximately eight points per vibration cycle. Images were acquired at 500 fps. In the diagram, the time variation of the light intensity is identical in all radial positions, except for a phase lag, and there is no evidence of the node-antinode configuration characteristic of standing waves.

In fact, the diagonally oriented stripes (which represent the time evolution of the fringes in the bottom half of Fig. 4), make it possible to identify a clear propagation direction: the waves travel inwards from the container wall towards its center (this could be also seen by direct inspection in the high speed videos). We deduce then that they are capillary waves generated by the vertically oscillating meniscus at the contact point between the wall and the liquid free surface [22]. Moreover, the time variation of the light intensity in any point of the ROI,

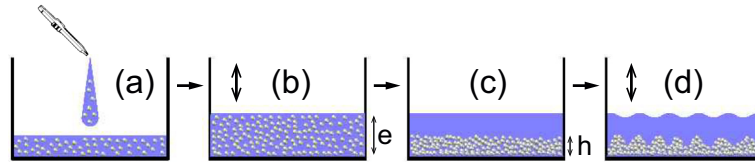


Fig. 3. Scheme of the patterned bed formation procedure. (a) The mixtures were prepared in an external reservoir, then a 9 ml sample was rapidly transferred to the container. Steps (b) and (c) are then performed to obtain a uniform bed. Finally, step d) takes place to generate the patterns.



Fig. 4. Upper half: Patterned bed at steady-state, ridges appear lighter and troughs darker. Lower half: the waves at the free surface as acquired by the beam-splitter. The white circles indicate the inner and outer limits of the ROI, while the characteristic lengthscale of the patterned bed λ_p (given by the ridge-to-ridge distance), and wavelength of the surface waves λ_w are shown by short vertical bars. For both figures: $f = 65$ Hz, $\Gamma = 1.03$, sample N° 2.

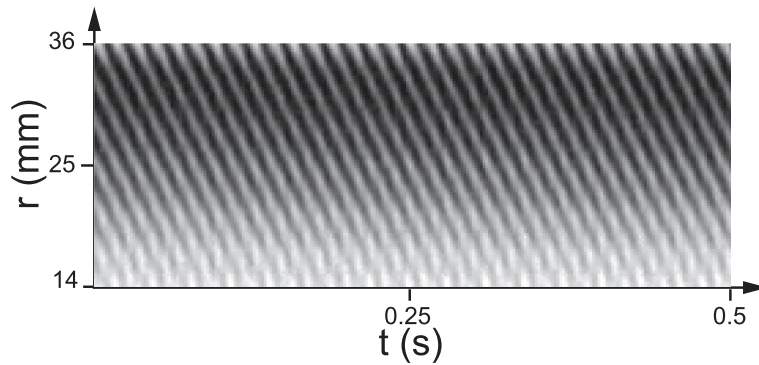


Fig. 5. Spatiotemporal diagram of the normalized light intensity reflected by the liquid free surface at $f = 65\text{ Hz}$. The orientation of the diagonal stripes indicate a clear propagation direction for the waves, that travel inwards from the container wall towards the center. This is for sample N° 2, and for a vibration frequency $f = 65\text{ Hz}$. Images were acquired at 500 fps.

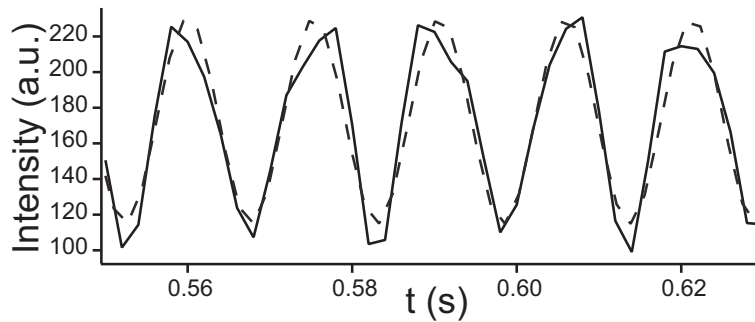


Fig. 6. Solid line: Time variation of the light intensity as measured in a position 24 mm away from the container center (from Fig. 5). A sinusoidal fit (dashed line) spanning 40 oscillation cycles yields a frequency of 65.35 Hz, in good agreement with the vibration frequency $f = 65\text{ Hz}$.

shown in Fig. 6 for a radial position near the external ROI limit, is well-fitted by a sinusoidal function, yielding a frequency parameter of 65.35 Hz, in good agreement with the $f = 65\text{ Hz}$ of the signal sent to the shaker, and measured by the accelerometer. This reveals the harmonic nature of the surface waves.

These results expand those of previous works [11,12,14], that found that the formation of patterns was due to the particle drift to the nodes of Faraday subharmonic waves. Regarding the type of waves involved, the relative weight of capillary to gravity effects, quantified by the ratio $4\pi^2\tau/g\rho_l\lambda_w^2$, ranges between 8 and 50 in our experiments, implying a strong prevalence of capillarity.

Fig. 7 shows the wavelength λ_w of the waves in the free surface, and the characteristic length λ_p of the patterned bed (respectively depicted

by the two small vertical bars of Fig. 4) as a function of the vibration frequency f , for experiment B.

The dispersion relation for harmonic capillary waves in an inviscid fluid, given by Eq. (1), is shown for reference, using $f = 65\text{ Hz}$, $\tau = 45\text{ Dyn/cm}$, $\rho_l = 1.03\text{ g/cm}^3$, $g = 980\text{ cm/s}^2$, and $e = 1.88\text{ cm}$; a very good agreement with λ_w is observed, in agreement with the hypothesis of meniscus waves. No significant variation of λ_w was observed when varying $\langle h \rangle$ within the range studied, being determined solely by f .

$$f = \sqrt{\frac{2\pi\tau}{\rho_l\lambda_w^3}} \quad (1)$$

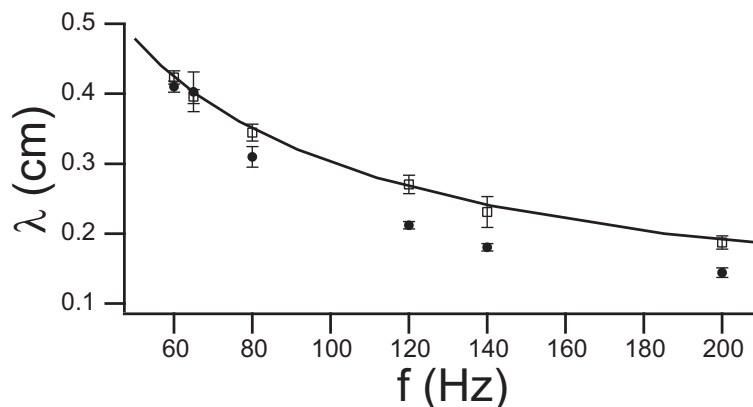


Fig. 7. Wavelengths λ_w (open squares) of the surface waves and λ_p (solid circles) of the particulate bed as a function of the vibration frequency f . Solid line shows the dispersion relation for harmonic capillary waves (Eq. (1)). Error bars quantify fluctuations over different radial positions.

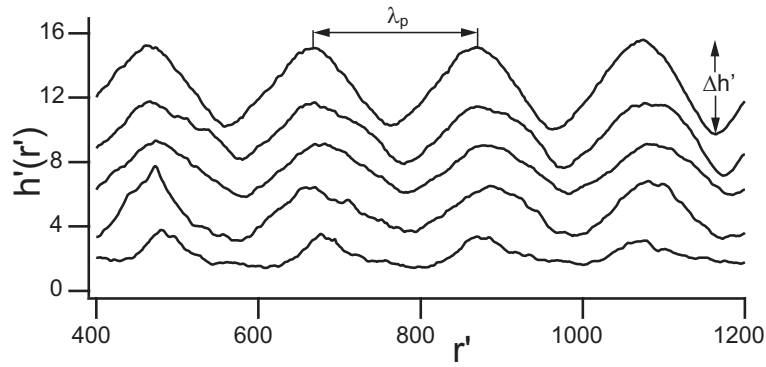


Fig. 8. Results of experiment A. Radial profiles of the dimensionless bed thickness h' as a function of r' , where $r' = r/a$ and $h' = h/a$. From bottom to top: Samples 1 to 5. This is for $f = 65$ Hz, $\Gamma = 1.03$, $e = 1.88$ mm = $94a$.

On the other hand, λ_p approaches λ_w for the lowest frequencies.
 4.2. Topography of the patterned bed

A photometric technique, developed in Appendix B, was used to map the smoothly varying local light intensity onto the local bed thickness. This made it possible to obtain 3D topographic maps of the patterned bed.

Taking advantage of the azimuthal symmetry, and, to provide results in terms of the particle radius a , results are shown as radial profiles of the dimensionless thickness $h'(r')$, where $h' = h/a$ and $r' = r/a$.

Fig. 8 shows the profiles $h'(r')$ for experiment A (the mean bed thickness $\langle h' \rangle$ increases from bottom to top). The profiles present an alternation of ridges and troughs, the distance between two ridges being λ_p .

It can be observed that the ridge-trough height $\Delta h'$, that quantifies the amplitude of the bed thickness variation, increases with $\langle h' \rangle$, while λ_p is independent.

Fig. 9 quantifies this variation, that presents a plateau for $5 < \langle h' \rangle < 8$, with the overall trend approximately following a linear behavior.

Regarding experiment B, Fig. 10 shows the profiles $h'(r')$ for different vibration frequencies.

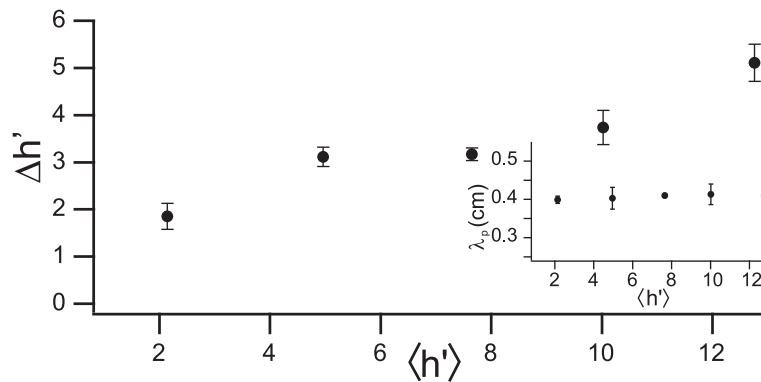


Fig. 9. Results of experiment A. Ridge-trough height $\Delta h'$, quantifying the amplitude of the thickness variation (or pattern roughness), as a function of $\langle h' \rangle$ for the same condition of Fig. 8. A monotonic increase is observed, except for a plateau for $5 < \langle h' \rangle < 8$. Note that, as $\langle h' \rangle$ increases, the bed surface gets closer to the liquid free surface. Inset: λ_p as a function of $\langle h' \rangle$.

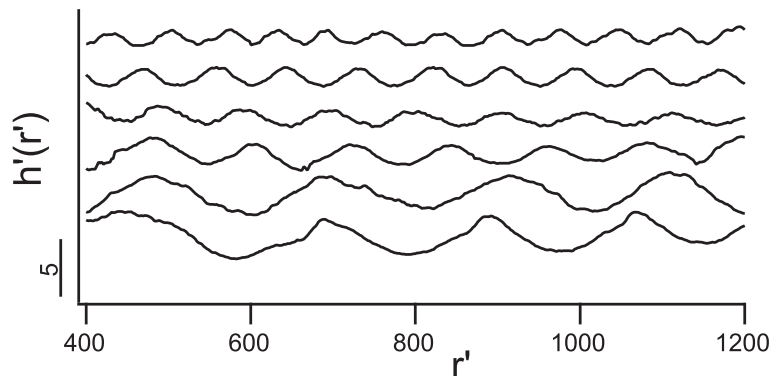


Fig. 10. Results of experiment B. Radial profiles $h'(r')$ for different frequencies f . The curves are vertically shifted for clarity, the mean value of h' is indicated as a reference, the short vertical bar at the left indicates $\Delta h' = 5$. From bottom to top: 60 Hz ($\langle h' \rangle = 4.8$), 65 Hz ($\langle h' \rangle = 4.7$), 80 Hz ($\langle h' \rangle = 5.2$), 120 Hz ($\langle h' \rangle = 5.4$), 140 Hz ($\langle h' \rangle = 4.2$) and 200 Hz ($\langle h' \rangle = 5.3$).

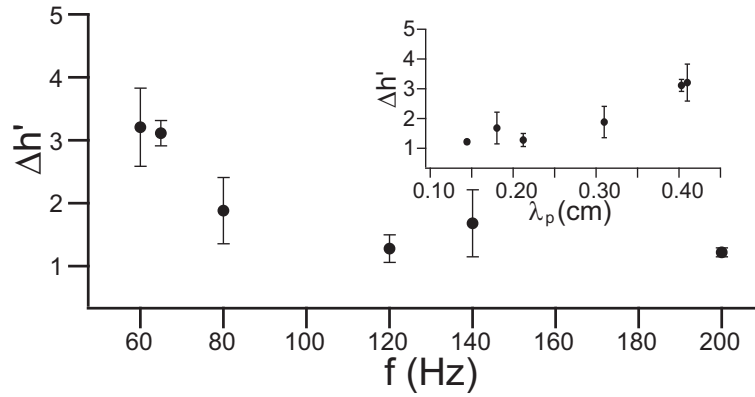


Fig. 11. Results of experiment B. Dimensionless ridge-trough height $\Delta h'$ as a function of f , for the profiles of Fig. 10. Inset: The same, but as a function of λ_p .

As in Fig. 7, it can be seen that λ_p can be modified by tuning the vibration frequency f , but, this also affects $\Delta h'$, that decreases markedly with f (Fig. 11). As for $\langle h' \rangle$, it remains nearly constant.

Note that, in all cases, the patterning of the bed is a smooth corrugation (note the spatial scales in Figs. 9 and 10).

5. Discussion

5.1. Underlying mechanisms

We summarize here some of the findings of the previous sections.

- The surface waves, and in particular, their wavelength λ_w , were unaffected by the presence of bed particles. We recall that, in our experiments, the bed thickness h was much smaller than the liquid layer thickness e .
- The characteristic lengthscale of the patterned bed λ_p approximated λ_w rather well, particularly for low frequencies.
- Both the characteristic length of the patterned bed λ_p , and the amplitude of the bed thickness variation Δh , depended on f , with λ_p typically 20 to 60 times larger than Δh . The smooth radial variation of the bed thickness implied by this ratio is consistent with the hypothesis of the photometric technique (see. Section Appendix B).

The first two findings show that the surface waves create the patterns in the particulate bed.

Having in mind that motion of the bed particles takes place when the destabilizing effect of the applied shear stress $\Theta = \eta \dot{\gamma}$ overcomes the stabilizing effect of gravity [34], we discuss our results in terms of the Shields number, that quantifies the relative weight of these two effects (Eq. (2)).

$$\Theta = \frac{\eta \dot{\gamma}}{[(\rho_p - \rho_l)g(2a)]} \quad (2)$$

A characteristic velocity for a liquid particle in the free surface can be estimated as $U_{surf} = A \omega/2$ [35], where A is the vibration amplitude and $\omega = 2 \pi f$ the angular frequency. Under the approximation of linear wave theory, this velocity attenuates downwards by a factor $\cosh(k_w z)$ [36], where z is the depth distance of a given point in the liquid to the free surface and $k_w = 2\pi/\lambda_w$. Then, at the bed surface, we have: $U_{bed} = \frac{A\pi f}{\cosh(k_w(e - \langle h \rangle))}$ where $e - \langle h \rangle$ is the thickness of the supernatant liquid layer above the bed. Finally, $\eta \dot{\gamma}_{bed} = \eta \frac{U_{bed}}{\delta}$, where

δ is the Stokes boundary layer thickness $\delta = \sqrt{\frac{\nu}{\pi f}}$ [35]. The estimated

Shields number Θ (Eq. (3)) then depends on $f^{3/2}$, through the shear velocity acting on the bed surface, and through the boundary layer size, while it depends on the mean bed thickness $\langle h \rangle$ through the attenuation factor $\cosh(k_w(e - \langle h \rangle))$.

$$\Theta = \frac{A(\pi f)^{3/2}(\nu)^{1/2}}{2a [\cosh(k_w(e - \langle h \rangle))] g [\rho_p/\rho_l - 1]} \quad (3)$$

Fig. 12 shows the amplitude of the thickness variation $\Delta h'$ as a function of Θ (from Eq. (3)) for all the experiments in the present work. The straight dotted line denotes the limiting value $\Delta h' = 1$, as $\Delta h'$ is expected to fluctuate of a particle radius as Θ tends to zero (uniform bed).

On the other hand, considering the amplitude of the thickness variation as a bed roughness, scaling in powers of Θ between 0.5 and 2 has been reported in the literature [37], which is consistent with our results (see. Fig. 12).

This suggests that it is the shear stress acting on the bed particles that controls the magnitude of $\Delta h'$, and then, that the influence of f over λ_p (through λ_w) is independent from its influence over $\Delta h'$ (through Θ).

The present experimental values of the Shields number are notably large compared to the existing literature, however we recall that, in most works, the liquid particle density contrasts are much higher than the one used in this work (typically $\rho_p/\rho_l - 1 = 1.7$ for a sand-water mixture, while $\rho_p/\rho_l - 1 = 0.02$ in this work), and particles are greater than the micrometric ones employed in the present work.

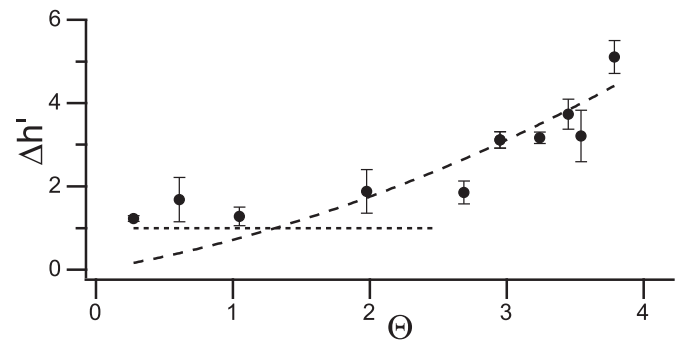


Fig. 12. Experiments A and B. Dimensionless ridge-trough height $\Delta h'$ as a function of Shields number Θ . The straight dotted line is $\Delta h' = 1$ ($\Delta h = a$), while the dashed curve is a quadratic function.

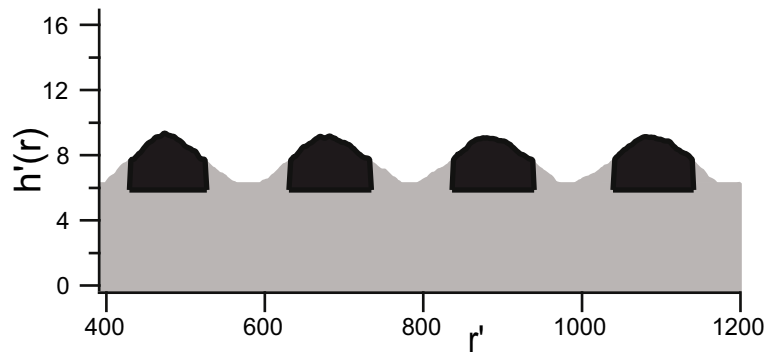


Fig. 13. Scheme depicting the definition of the localization efficiency parameter L , showing, in a cut view, the volume of particles within the ridges that are considered as localized (in black), and the rest of the particles in grey, for sample N° 3 at $f = 65$ Hz. Note that L is actually calculated using the 3D representation of the patterned bed.

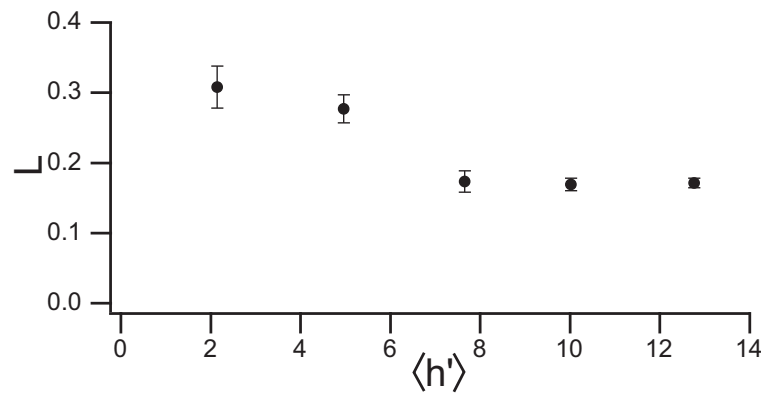


Fig. 14. Results of experiment A. Localization efficiency parameter L as a function of $\langle h' \rangle$ at $f = 65$ Hz. Error bars quantify fluctuations over ridges in different radial positions.

5.2. Localization efficiency

As stated in Sec. 1, several authors [11,12,14,15] have used the liquid template technique to localize organic and inorganic particles over a substrate, creating an assembly. They frequently employed cells of similar sizes than our particles (10–100 μm), focusing mainly on biological aspects that come on the scene once a first assembly is achieved. It becomes then of technological interest to evaluate the localization efficiency in our experiments, analyzing its dependence on the quantity of particles (quantified by $\langle h' \rangle$) and on the pattern characteristic lengthscale λ_p , as these two parameters control the geometrical structure of the assembly.

Quantifying the localization efficiency is not straightforward. For example, Saylor and Kinard [13], could, in their numerical study, track

individual particle trajectories, and so they used the standard deviation of the particle final deposition location about an accumulation point as a localization efficiency parameter. We have preferred to take into account the fact that the assembly is a patterned bed, retaining a 3D picture of the bed topography.

Defining the radial position of the higher points of the bed (the tip of the ridges) as accumulation planes, and the points midway between two accumulation planes as depletion planes (coincident in many cases with the bottom of a trough but not necessarily), we consider as localized the particles that fulfil the two following conditions:

- 1) They are closer to an accumulation plane than to a depletion plane.
- 2) They are situated above the level of the bottom of the troughs.

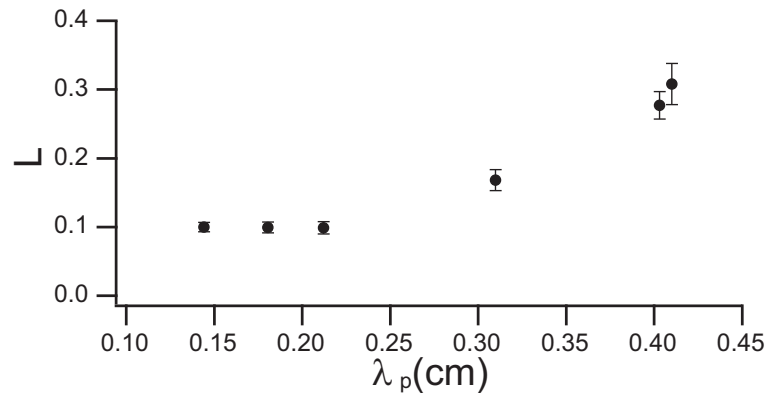


Fig. 15. Results of experiment B. Localization efficiency parameter L as a function of λ_p for sample N° 2. The curve shows a plateau for higher frequencies, with a marked increase for $\lambda_p > 0.25$ (lower frequencies). The parameter L increases as λ_p increases.

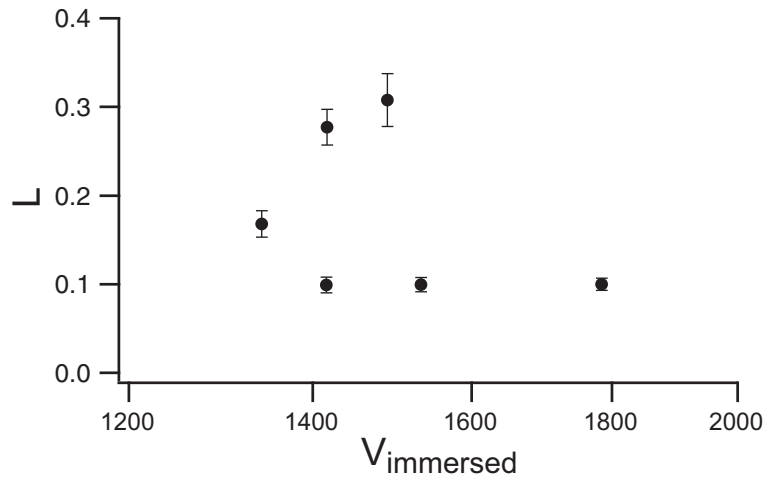


Fig. 16. Localization efficiency L as a function of $V_{immersed}$.

The localization efficiency L is then calculated as the ratio of the volume occupied by the bed particles that are localized to the volume occupied by all the particles (the volume under the bed surface). Fig. 13 depicts this definition by showing a cut view of the bed with the volume of localized particles coloured in black, while the volume of non-localized particles is coloured in grey, for sample N° 3, and at $f = 65$ Hz.

Note that the definition of such a parameter L remains arbitrary and should be modified if studying different types of patterns. In the following, we study the dependence of L on the experimental parameters, with focus in assembly design.

Fig. 14 shows the variation of L as a function of the dimensionless mean bed thickness $\langle h' \rangle$. Despite the fact that $\Delta h'$ increases with $\langle h' \rangle$ (Fig. 9), L decreases from a value of 0.3 with it until reaching a plateau. A localization efficiency that decreases with the quantity of particles in the system has already been reported in liquid templates: Chen et al. [14] found that their spheroids aligned themselves in line assemblies, whose width increased as the quantity of particles increased, then yielding a lower localization efficiency. Both results imply that the localization of fewer particles is more efficient.

On the other hand, Fig. 15 shows the variation of L with the pattern lengthscale λ_p . An increase can be observed for $\lambda_p > 0.25$, favouring the choice of larger lengthscales for obtaining better localization efficiencies.

Previous studies by other authors [30] in dry particle systems showed a data collapse when the assembly efficiency was plotted as a function of the vibration velocity amplitude, instead of as a function of the (more frequently used) vibration acceleration Γ . For dry systems, the vibration velocity amplitude V_{dry} is defined in Eq. (4):

$$V_{dry} = A(2\pi f) / \sqrt{2ag} \quad (4)$$

For immersed systems, the velocity amplitude can be expressed as shown in Eq. (5), where the velocity of a particle falling freely under gravity $\sqrt{2ag}$ is replaced by the Stokes velocity $V_{St} = 2a^2g(\rho_p - \rho_l) / 9\eta$. All parameters are defined in Table 1.

$$V_{immersed} = A(2\pi f) / V_{St} \quad (5)$$

Fig. 16 shows the variation of the localization efficiency L as a function of $V_{immersed}$. A data collapse for different frequencies is not observed, in contrast with dry granular systems [30].

6. Conclusions

We have studied systematically the formation of particulate patterns in liquid templates.

By visualizing simultaneously the particles bed and the free liquid surface, we conclude that, in our experimental conditions, the waves that conform the template are harmonic travelling waves, complementing previous results that examined subharmonic Faraday waves as the driver for particle assembly. The waves travel inwards from the container walls to the center, favouring the hypothesis of capillary waves generated by the meniscus at the boundary [22]. Moreover, a good agreement of the surface wavelength with the capillary dispersion relation is found.

It is shown that, by tuning this surface wavelength through the choice of an appropriate vibration frequency, it is possible to control, in reasonable degree, the characteristic scale of the patterned bed. Regarding the underlying mechanisms, by studying the topographic profiles of the bed, we find that the amplitude of the thickness variations increases as the mean bed thickness increases, and as the vibration frequency decreases. Both dependences are well accounted for by expressing results in terms of a Shields number. This suggests that the mobility of the particles is due to the existence of an erosive process driven by the shear stress acting on the bed surface.

To verify that the influence of the vibration frequency over the pattern characteristic length is independent from its influence over the pattern roughness (both are two important constructive parameters in the assembly design), experiments in which the vibration frequency is varied while the Shields number is kept constant might be performed. For a given frequency, the patterns became rapidly blurred as the vibration acceleration values departed from those used in this work, due to global recirculation currents. This means that this verification constitutes an experimental challenge, which might be subject of future work.

It is likely that the particle size should also be taken into account, because the Shields number, that drives particle motion, depends on it. In this work we've studied a single particle size. In the same direction, the density contrast between fluid and particles affects the capacity of the waves to mobilize particles.

In addition, our results show that the localization efficiency depends both on the quantity of particles and on the pattern characteristic lengthscale, both dependences should be taken into account during assembly design.

Finally, comparing particle assembly in dry and immersed particulate systems, the patterns generated by the liquid templates present some similarity with those found in the dry case (see, for example, Fig. 6 a) in [2]), but the presence of the liquid template strongly

modifies the mechanisms of interactions among particles and container [38], and the vibration conditions seem to affect both systems differently [30].

Further studies should address a detailed description and understanding of the pattern formation mechanism and dynamics, for example by performing PIV (Particle Image Velocimetry) measurements in different stages of the formation of the patterns.

Nomenclature

a	Particles radius (20 μm)
f	Vibration frequency (Hz)
A	Vibration amplitude (mm)
Γ	Reduced acceleration
d	Container diameter (7.8 cm)
H	Container height (4.5 cm)
ρ_l	Liquid density (1.03 g/cm ³)
η	Liquid absolute viscosity (0.001 Pa. s)
τ	Liquid surface tension (45 Dyn/cm)
ρ_p	Density of the particles (1.05 g/cm ³)
Φ	Mixture sample volume fraction (%)
Φ_{RLP}	Random close packing volume fraction (58%)
V	Mixture sample volume (9 ml)
V_{dry}	Dry vibration velocity amplitude
$V_{immersed}$	Immersed vibration velocity amplitude
e	Mixture layer thickness (1.88 mm)
m_p	Particle mass (g)
m_f	Liquid mass (g)
h	Mean bed thickness (mm)

h'	Dimensionless mean bed thickness (a)
I_N	Normalized light intensity
λ_p	Characteristic length of the patterned bed (cm)
λ_w	Wavelengths of the free surface waves (cm)
ν	Kinematic viscosity of fluid (cm ² /s)
$\Delta h'$	Ridge-trough height (a)
δ	Stokes boundary layer thickness (cm)
ω	Angular velocity (rad/s)
Θ	Shields number
$\dot{\gamma}$	Shear velocity(1/s)

Declaration of Competing Interest

The authors declare that they have no known competing financial interests or personal relationships that could have appeared to influence the work reported in this paper.

Acknowledgements

The authors acknowledge the support from PIP CONICET 11220130100230CO, PICT MiNcyT 2013-2584, UBACYT 20020150200142BA and 20020170200066BA, scholarships for university teachers awarded by SENESCYT-ECUADOR and we thank to Gustavo Bongiovanni for his help in the electronic settings used to measure the parameters. We thank José-Eduardo Wesfreid, Jean-Christophe Géminard, Germán Drazer and María Alejandra Aguirre for fruitful discussions. Also, we would like to thank Georges Gauthier.

Appendix A. Regimes and choice of the vibration frequency and acceleration

A set of preliminary exploratory measurements was performed to determine the working frequency and acceleration for the experiments by inspecting the particle patterns. Regarding the influence of the acceleration at fixed frequency f , for example, for $f = 65$ Hz, $e = 1.88$ mm and $0.1 < \Gamma < 1.03$, the particle patterns were the concentric alternation of ridges and troughs shown in Fig. 4. For $1.04 < \Gamma < 1.26$, the particle patterns presented complex star-shaped patterned beds with some resuspension (the surface waves also lost the circular symmetry), while for $\Gamma > 2$ particles resuspended and no pattern formation was observed (the surface waves became non-stationary).

On the other hand, for example, when Γ was held constant at a value of 1.03 and f varied, the localization of particles in rings was poorer as f increased from 70 Hz, while recirculation flow begun to distort the rings as f decreased from 60 Hz.

In view of these observations, it became evident that a quantitative characterization of the particle patterns was only possible in situations in which they kept a concentric annular structure. Because of this, we chose to work, for each frequency, in the maximum value of Γ that maintained that condition, achieving the clearest particle patterns for each frequency. These are the pair values (f, Γ) presented in Table 3 for experiment B, and the pair ($f = 65$ Hz, $\Gamma = 1.03$), for experiment A.

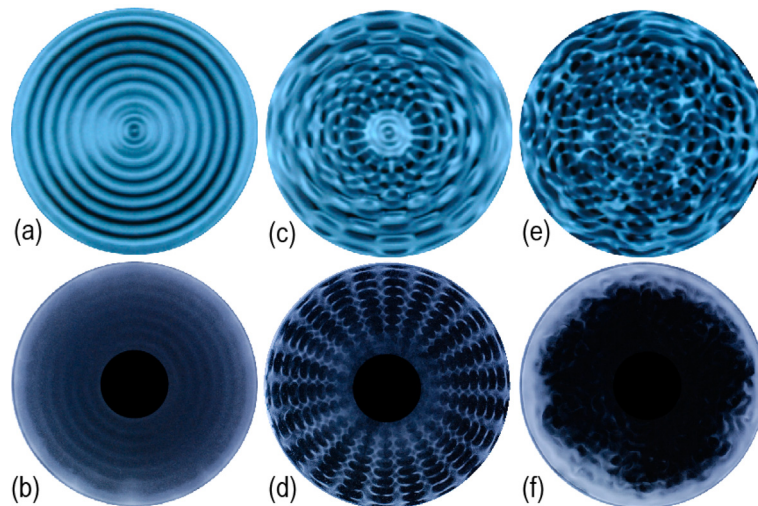


Fig. 17. Surface waves (top row) and particle patterns (bottom row) for $f = 65$ Hz and different ranges of Γ . Left: $0.1 - 0.2 < \Gamma < 1.03$. Center: $1.04 < \Gamma < 1.26$ (some particle resuspension occurred). Right: $\Gamma > 1.3$ (the surface waves were non-stationary and significant particle resuspension occurred).

Appendix B. Calibration curve

To study the topography of the patterned beds, we employed a technique based on monotonic increase of the light intensity captured by the camera with the local bed thickness. This technique is inspired in that employed in reference [39, 40] and makes use of a calibration curve constructed over known reference values of uniform bed thicknesses h_k , and the corresponding measured light intensity for each pixel $I_k(x, y)$ in the images, to obtain a map of bed thicknesses $h(x, y)$.

To avoid the influence of any spatial non-uniformity in the illumination, mapping was performed on a pixel by pixel basis, each pixel having its own calibration curve. Similarly, to avoid the influence of possible time fluctuations in the illumination, intensities were normalized by a reference value reference zone, located outside the container, in the images.

For a uniform bed, $h'_k = \frac{h_k}{a}$ is related to Φ_k according to:

$$h'_k = \frac{e \Phi_k}{a \Phi_{RLP}} \quad (\text{A.1})$$

where h'_k is the dimensionless bed thickness, a is the radius of particles, e is the mixture layer thickness, Φ_k is the mixture volume fraction and $\Phi_{RLP} \sim 58\%$, corresponding to a bulk volume fraction of particles slowly settled in a liquid [26,41].

Steps a), b) and c) of section 3 were reproduced to obtain the uniform beds, and then, images of the light intensity were acquired. In order to achieve a good sampling of h'_k in the range of thicknesses sampled by the patterned beds (taking into account the ridges and troughs), we extended the range of Φ_k , using 2%, 4%, 6%, 8%, 10%, 12%, 16%, 20%, 24%.

In our point of view, under the assumption of smooth spatial variation of the bed thickness in the direction perpendicular to the optical axis, the technique provides acceptable accuracy. In Sec. 4.2 it is shown that this condition is reasonably satisfied. A source of error exists due the fact that vibration (step d) of the formation procedure of the patterned beds) might increase the bulk volume fraction of the bed. According to the literature [26], this variation might be of approximately 3%.

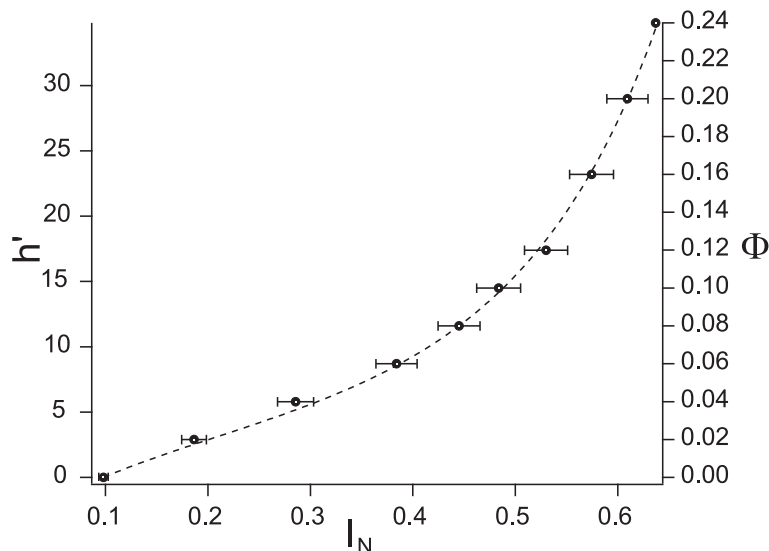


Fig. 18. Symbols: Example of the calibration curve relating the measured light intensity I_N with the local dimensionless bed thickness h . Right axis is the mixture volume fraction that corresponds (after settling) to each bed thickness. Solid line: Fit by the expression of Eq. (7) that is used to interpolate the intensities. Horizontal bars indicate the magnitude of the spatial fluctuation of I_N .

Fig. 18 shows the variation of the dimensionless bed thickness $\frac{h'_k}{a}$ with the normalized light intensity I_k (averaged over the ROI) and a fit by the analytical expression of Eq. (7), used to interpolate the calibration values. $W_0; W_1; W_2; W_3$ are adjustable coefficients. $W_0 = 0.09 \pm 0.02$, $W_1 = 23 \pm 2$, $W_2 = 6 \pm 3$, $W_3 = -3.0000 \pm 6 e - 5$

$$h' = W_1(I_N - W_0) \exp\{W_2(I_N)^2 + W_3 I_N\} \quad (\text{A.2})$$

The technique yielded a bed thickness map $h'(x, y)$. In view of the circular symmetry of the patterns, an azimuthal average was performed to obtain a radial bed thickness profile $h'(r')$ for each experiment these are the profile presented in Section 4.2.

References

- [1] I. Aranson, L. Tsimring, Patterns and collective behavior in granular media: theoretical concepts, *Rev. Mod. Phys.* 78 (2) (2006) 641–692, <https://doi.org/10.1103/RevModPhys.78.641>.
- [2] P. Umbanhowar, F. Melo, H. Swinney, Periodic, aperiodic, and transient patterns in vibrated granular layers, *Physica A* 249 (1–4) (1998) 1–9, [https://doi.org/10.1016/S0378-4371\(97\)00425-1](https://doi.org/10.1016/S0378-4371(97)00425-1).
- [3] S. Tasoglu, C.H. Yu, V. Liaudanskaya, S. Guven, C. Migliaresi, U. Demirci, Magnetic levitational assembly for living material fabrication, *Adv. Healthc. Mater.* 4 (10) (2015) 1469–1476, <https://doi.org/10.1002/adhm.201500092>.
- [4] Y. Yu, K. Moncal, J. Li, W. Peng, I. Rivero, J. Martin, I. Ozbolat, Three-dimensional bioprinting using self-assembling scalable scaffold-free “tissue strands” as a new bioink, *Sci. Rep.* 6 (2016) <https://doi.org/10.1038/srep28714>.
- [5] G. Yang, H. Lin, B.B. Rothrauff, S. Yu, R.S. Tuan, Multilayered polycaprolactone/gelatin fiber-hydrogel composite for tendon tissue engineering, *Acta Biomater.* 35 (2016) 68–76, <https://doi.org/10.1016/j.actbio.2016.03.004>.
- [6] J.J. Juárez, M.A. Bevan, Feedback controlled colloidal self-assembly, *Adv. Funct. Mater.* 22 (18) (2012) 3833–3839, <https://doi.org/10.1002/adfm.201200400>.
- [7] M. Wang, L. He, Y. Yin, Magnetic field guided colloidal assembly, *Mater. Today* 16 (4) (2013) 110–116, <https://doi.org/10.1016/j.mattod.2013.04.008>.

- [8] S. Wollmann, R.B. Patel, A. Wixforth, H.J. Krenner, Ultrasonically assisted deposition of colloidal crystals, *Appl. Phys. Lett.* 105 (3) (2014) 031113, <https://doi.org/10.1063/1.4891171>.
- [9] C.E. Owens, C.W. Shields, D.F. Cruz, P. Charbonneau, G.P. López, Highly parallel acoustic assembly of microparticles into well-ordered colloidal crystallites, *Soft Matter* 12 (3) (2016) 717–728, <https://doi.org/10.1039/C5SM02348C>.
- [10] S. Watanabe, M.T. Miyahara, Particulate pattern formation and its morphology control by convective self-assembly, *Adv. Powder Technol.* 24 (6) (2013) 897–907, <https://doi.org/10.1016/j.apt.2013.06.001>.
- [11] S. Takagi, V. Krinsky, A. Pimir, C. Frelin, The use of Faraday instability to produce defined topological organization in cultures of mammalian cells, *Int. J. Bifurcation Chaos* 12 (9) (2002) 2009–2019, <https://doi.org/10.1142/S0218127402005662>.
- [12] P.H. Wright, J.R. Saylor, Patterning of particulate films using Faraday waves, *Rev. Sci. Instrum.* 74 (9) (2003) 4063–4070, <https://doi.org/10.1063/1.1602936>.
- [13] J.R. Saylor, A.L. Kinard, Simulation of particle deposition beneath Faraday waves in thin liquid films, *Phys. Fluids* 17 (4) (2005) 047106, <https://doi.org/10.1063/1.1884111>.
- [14] P. Chen, S. Güven, O.B. Usta, M.L. Yarmush, U. Demirci, Biotunable acoustic node assembly of organoids, *Adv. Healthc. Mater.* 4 (13) (2015) 1937–1943, <https://doi.org/10.1002/adhm.201500279>.
- [15] V. Serpooshan, P. Chen, H. Wu, S. Lee, A. Sharma, D.A. Hu, S. Venkatraman, A.V. Ganesan, O.B. Usta, M. Yarmush, F. Yang, J.C. Wu, U. Demirci, S.M. Wu, Bioacoustic-enabled patterning of human iPSC-derived cardiomyocytes into 3D cardiac tissue, *Biomaterials* 131 (2017) 47–57, <https://doi.org/10.1016/j.biomaterials.2017.03.037>.
- [16] B. Thomas, A.M. Squires, Confirmation of Faraday's explanation of bunkering in vibrated granular beds, *Powder Technol.* 100 (2) (1998) 200–210, [https://doi.org/10.1016/S0032-5910\(98\)00141-7](https://doi.org/10.1016/S0032-5910(98)00141-7).
- [17] L. Li, P. Wu, S. Zhang, L. Wang, Patterns of particle convection in a mono-size granular system under coupling vibration and airflow, *Powder Technol.* 342 (2019) 954–960, <https://doi.org/10.1016/j.powtec.2018.10.051>.
- [18] P. Blondeaux, Sand ripples under sea waves Part 1. Ripple formation, *J. Fluid Mech.* 218 (HY11) (1990) 1–17, <https://doi.org/10.1017/S0022112090000908>.
- [19] G. Rousseaux, A. Stegner, J.E. Wesfreid, Wavelength selection of rolling-grain ripples in the laboratory, *Phys. Rev. E* 69 (3) (2004) <https://doi.org/10.1103/PhysRevE.69.031307> 031307 (Mar 2004).
- [20] G. Rousseaux, H. Yoshikawa, A. Stegner, J.E. Wesfreid, Dynamics of transient eddy above rolling-grain ripples, *Phys. Fluids* 16 (4) (2004) 1049–1058, <https://doi.org/10.1063/1.1651482>.
- [21] F. Pedocchi, M.H. García, Ripple morphology under oscillatory flow: 1. Prediction, *J. Geophys. Res. Oceans* 114 (C12) (2019) <https://doi.org/10.1029/2009JC005354>.
- [22] S. Douady, Experimental study of the Faraday instability, *J. Fluid Mech.* 221 (5) (1990) 383–409, <https://doi.org/10.1017/S0022112090003603>.
- [23] K. Zhang, T. Chen, L. He, Damping behaviors of granular particles in a vertically vibrated closed container, *Powder Technol.* 321 (2017) 173–179, <https://doi.org/10.1016/j.powtec.2017.08.020>.
- [24] G.A. Voth, B. Bigger, M.R. Buckley, W. Losert, M.P. Brenner, H.A. Stone, J.P. Gollub, Ordered clusters and dynamical states of particles in a vibrated fluid, *Phys. Rev. Lett.* 88 (23) (2002), 234301. (May 2002) <https://doi.org/10.1103/PhysRevLett.88.234301>.
- [25] C. Hanotin, S. Kiesgen de Richter, P. Marchal, L.J. Michot, C. Baravian, Vibration-induced liquefaction of granular suspensions, *Phys. Rev. Lett.* 108 (2012) 198301, (May 2012) <https://doi.org/10.1103/PhysRevLett.108.198301>.
- [26] S.K. de Richter, C. Hanotin, P. Marchal, S. Leclerc, F. Demeurie, N. Louvet, Vibration-induced compaction of granular suspensions, *Eur. Phys. J. E* 38 (2015) 1–9, (07 2015) <https://doi.org/10.1140/epje/i2015-15074-7>.
- [27] N. Ku, C. Hare, M. Ghadiri, M. Murtagh, R.A. Haber, Effect of mechanical vibration on the size and microstructure of titania granules produced by auto-granulation, *Powder Technol.* 286 (2015) 223–229, <https://doi.org/10.1016/j.powtec.2015.05.041>.
- [28] O. Pouliquen, M. Nicolas, P. Weidman, Crystallization of non-brownian spheres under horizontal shaking, *Phys. Rev. Lett.* 79 (19) (1997) 3640–3643, <https://doi.org/10.1103/PhysRevLett.79.3640>.
- [29] A. Yu, X. An, R. Zou, R. Yang, K. Kendall, Self-assembly of particles for densest packing by mechanical vibration, *Phys. Rev. Lett.* 97 (26) (2006) <https://doi.org/10.1103/PhysRevLett.97.265501>.
- [30] R. Amirifar, K. Dong, Q. Zeng, X. An, Self-assembly of granular spheres under one-dimensional vibration, *Soft Matter* 14 (48) (2018) 9856–9869, <https://doi.org/10.1039/c8sm01763h>.
- [31] C. Lesaffre, V. Mineau, D. Picart, H. Van Damme, Densification under vibration of a saturated granular packing, *Comptes Rendus de l'Academie des Sciences - Series IV: Physics, Astrophysics* 1 (5) (2000) 647–653, [https://doi.org/10.1016/S1296-2147\(00\)01089-1](https://doi.org/10.1016/S1296-2147(00)01089-1).
- [32] G. Gauthier, P. Gondret, Compaction of liquid immersed granular packings by small upward flows, *Phys. Rev. Fluids* 4 (2019) 074308, (Jul 2019) <https://doi.org/10.1103/PhysRevFluids.4.074308>.
- [33] G. Farrell, K. Martini, N. Menon, Loose packings of frictional spheres, *Soft Matter* 6 (13) (2010) 2925–2930, <https://doi.org/10.1039/c0sm00038h>.
- [34] M. Ouriemi, P. Aussillous, M. Medale, Y. Peysson, E. Guazzelli, Determination of the critical Shields number for particle erosion in laminar flow, *Phys. Fluids* 19 (6) (2007) <https://doi.org/10.1063/1.2747677>.
- [35] G. Rousseaux, J. Kruithof, P. Jenffer, J.E. Wesfreid, Oscillation-induced sand ripples in a circular geometry, *Phys. Rev. E* 78 (2008) 016302, (Jul 2008) <https://doi.org/10.1103/PhysRevE.78.016302>.
- [36] Chapter 8 the generation and dissipation of waves, in: P.H. LeBlond, L.A. Mysak (Eds.), *Waves in the Ocean*, Elsevier 1978, pp. 451–560, [https://doi.org/10.1016/S0422-9894\(08\)70821-3](https://doi.org/10.1016/S0422-9894(08)70821-3), Vol. 20 of Elsevier Oceanography Series.
- [37] B. Camenen, M. Larson, A. Bayram, Equivalent roughness height for plane bed under oscillatory flow, *Estuar. Coast. Shelf Sci.* 81 (3) (2009) 409–422, <https://doi.org/10.1016/j.ecss.2008.11.019>.
- [38] E. Guazzelli, J. Morris, A physical introduction to suspension dynamics, *Phys. Introduction Suspension Dyn.* (2011) 1–229, <https://doi.org/10.1017/CBO9780511894671>.
- [39] A. Boschan, H. Auradou, I. Ippolito, R. Chertcoff, J.-P. Hulin, Miscible displacement fronts of shear thinning fluids inside rough fractures, *Water Resour. Res.* 43 (10) (2006) <https://doi.org/10.1029/2006WR005324>.
- [40] A. Boschan, M. Poblete, Y. Roht, I. Ippolito, R. Chertcoff, Light transmission measurement of solute dispersion in non-brownian suspension flow, *EPJ Appl. Phys.* 65 (1) (2014) <https://doi.org/10.1051/epjap/2013130340>.
- [41] P. Snabre, B. Poulligny, C. Metayer, F. Nadal, Size segregation and particle velocity fluctuations in settling concentrated suspensions, *Rheol. Acta* 48 (10) (2008) 855–870, <https://doi.org/10.1007/s00397-008-0338-42008>.